Electronic Supplementary Information

Enhancing the reaction kinetics and structural stability of high-voltage LiCoO$_2$ via polyanionic species anchoring

Wei Zheng,[a] Gemeng Liang,*[a] Hao Guo,[b] Jingxi Li,[a] Jinshuo Zou,[a] Jodie A. Yuwono,[a] Hongbo Shu,*[c] Shilin Zhang,[a] Vanessa K. Peterson,[d] Bernt Johannessen,[ef] Lars Thomsen,[e] Wenbin Hu[b] and Zaiping Guo*[a]

[a]School of Chemical Engineering, The University of Adelaide, Adelaide, South Australia 5005, Australia

[b]School of Materials Science and Engineering, Tianjin University, Tianjin 300072, China

[c]China National Base for International Science & Technology Cooperation of New Energy Equipment, Hunan Province Key Laboratory for Electrochemical Energy Storage and Conversion, School of Chemistry, Xiangtan University, Xiangtan, Hunan 411105, China

[d]Australian Centre for Neutron Scattering, Australian Nuclear Science and Technology Organisation, Sydney, New South Wales 2234, Australia

[e]Australian Synchrotron, Australian Nuclear Science and Technology Organisation, Clayton, Victoria 3168, Australia

[f]Institute for Superconducting and Electronic Materials, University of Wollongong, Wollongong, New South Wales 2522, Australia

Email: gemeng.liang@adelaide.edu.au (G. Liang); hongboshu@xtu.edu.cn (H. Shu); zaiping.guo@adelaide.edu.au (Z. Guo)

Experimental Section

Materials Synthesis

Pristine $LiCoO_2$ samples were purchased from Canrd New Energy Technology Co. Ltd. N@P was synthesized using an ion-exchange method followed by high-temperature treatment. In detail, 0.1 mol $LiCoO_2$ was dispersed into a 5 M NH_4Cl (Sigma Aldrich, 99%) solution and continuously stirred for two days. The mixture was then filtered and washed with deionized water for twice and dried at 80 °C for 24 h, after which the dried precursors were mixed and milled with 1 wt.% Li_3PO_4 (Sigma Aldrich, 99%). Finally, the mixed precursors sintered at 800 °C for 4 h. Meanwhile, series of samples with different experimental parameters were prepared for comparison, including sintering temperatures of 700 °C (N@P-700 °C) and 900 °C (N@P-900 °C), duration time for the exchange process of 1 day (N@P-1 day) and 3 days (N@P-3 days), incorporated ratio of Li_3PO_4 for 0.5 wt.% (N@P-0.5) and 2 wt.% (N@P-2.0), sample with separate NH_4Cl solution and sintering treatment (@N), and samples with separate 1 wt.% Li_3PO_4 and sintering treatment (@P).

Material characterization

A lab Rigaku MiniFlex 600 X-ray diffractometer was employed to obtain X-ray diffraction (XRD) data with a Cu Kα radiation source λ = 1.5046 Å at 40 kV and 25 mA. Neutron powder diffraction (NPD) data were collected on Echidna,[1] the high-intensity neutron powder diffractometer at the Open Pool Australian Light water (OPAL) research reactor at the Australian Nuclear Science and Technology Organisation (ANSTO) (Sydney, Australia). The neutron wavelength was determined to be 1.62156(9) Å using data for the $La^{11}B_6$ National Institute of Standards and Technology (NIST) standard reference material 660b. High-resolution NPD data were collected in the angular range 15-160º with the step size of 0.125º. Rietveld refinement of the layered structure against NPD was conducted using the GSAS-II software,[2] in which the refined parameters included background coefficients, zero shift, peak shape coefficients, lattice parameters, scale factors, and isotropic atomic displacement

parameters. Scanning electron microscopy (SEM) images were gained using a FEI QUANTA 450 electron microscope. The images of aberration-corrected scanning transmission electron microscopy (STEM) with Energy Dispersive Spectroscopy (EDS) in high-angle annular dark-field (HAADF) and annular bright-field (ABF) modes were performed on a FEI Titan Themis 80-200 at the working voltage of 200 kV. X-ray photoelectron spectroscopy (XPS) data was tested by a Thermo Fisher KAlpha system. PerkinElmer Frontiers instrument with an attenuated total reflectance (ATR) attachment was used to collect the Fourier-transform infrared spectroscopy (FT-IR) spectra. Raman tests were conducted by Horiba LabRam Evolution spectrometer. The gas generation was analyzed by operando differential electrochemical mass spectrometry (DEMS, a Hiden HPR-20 gas analysis system) and the carrier gas was Argon with a speed of 0.8 mL/min. The cell was cycled in the voltage range of 3.0 - 4.65 V and at the current of 20 mA g^{-1}.

Battery assembly

Active materials, super P, and polyvinylidene difluoride (PVDF) with a weight ratio of 8:1:1, were homogeneously mixed and dispersed in N-methyl-2-pyrrolidone (NMP) solution. The uniform slurry was coated on Al foil and dried at 110 °C for 12 h in a vacuum oven. The electrodes were cut into disks. CR2032-type coin cells were assembled in an Ar glovebox. Li foil was used as the counter electrode, Celgard 2400 polypropylene film was applied as separator, and 1 M LiPF$_6$ in a 1:1 volume ratio mixture of ethylene carbonate (EC) and dimethyl carbonate (DMC) was as electrolyte in the battery assembly. Pouch cells were assembled using Li metal foil as counter electrode. A NEWARE battery testing system (CT-4008T-5V10mA-164 Shenzhen, China) was used to characterize the charge-discharge performance in the voltage range of 3.0 – 4.6 V. Galvanostatic intermittent titration technique (GITT) was performed with charging at 54.8 mA g^{-1} for 10 min and relaxation for 60 min. Cyclic voltammetry (CV) measurements were conducted using a Bio-Logic VMP3 workstation. The lithium diffusion coefficient (D$_{Li}$) based on CV test was calculated by the Randles-Sevcik

equation[3]:

$$i_P = (2.69 \times 10^5) n^{3/2} A D_{Li}^{1/2} V^{1/2} \Delta C_{L_i}$$

in which i_p corresponds to the peak current (A), n represents the number of electrons per reaction species, A is the surface area of the tested electrode, D_{Li} is the apparent diffusion coefficient of Li ($cm^2 s^{-1}$), v is the scan rate ($V s^{-1}$), and ΔC_{Li} is the change in lithium-ion concentration ($mol cm^{-3}$).

Ex/in situ measurements with synchrotron and neutron beams

Ex situ synchrotron soft X-ray absorption spectroscopy (Soft-XAS), hard X-ray absorption spectroscopy (XAS) and *in situ* synchrotron-based X-ray diffraction characterizations (sXRPD) were conducted at the Australian Synchrotron (Melbourne, Australia).

For *ex-situ* measurements, electrodes were extracted from coin cell and washed with DMC before testing. Co *L* and O *K* edge spectra were obtained in total electron yield mode (TEY) at soft X-ray (SXR) beamline and processed using the Igor Pro 8 software with QANT.[4] Co *K* edge data includes X-ray absorption near-edge structure (XANES) and extended X-ray absorption fine structure (EXAFS) spectra, which were collected at the medium energy X-ray absorption spectroscopy 1 (MEX1) beamline in transmission mode, with normalized data processed using the ATHENA software.[5]

In situ sXRPD measurements were conducted at the Powder Diffraction beamline. The synchrotron beam wavelength was determined to be 0.688726(1) Å using the $La^{11}B_6$ standard reference material 660b. A CR2032 coin cell was fabricated as described earlier, and holes approximately 4 mm in diameter punched through both positive and negative side caps to facilitate synchrotron beam transmission. To prevent any contact with air, aluminum and copper conductive tape (3M®) were applied to cover the hole on the positive and negative caps, respectively. Coin cells were tested in the voltage range 3.0 - 4.6 V at the current density of 27.4 mA g^{-1}. Diffraction patterns were recorded with an exposure time of 3 minutes and with an interval between acquisitions

of 828 s.

In-operando NPD data were collected using Wombat,[6] the high-intensity neutron diffractometer at ANSTO (Sydney, Australia). 1 Ah pouch cells with Li foil counter electrodes were fabricated for these experiments. The neutron wavelength was determined to be 2.41358(3) Å using the $La^{11}B_6$ standard reference material 660b. Diffraction data were captured for 4-minute exposure time and the angular range of 20º to 130º. Pouch cells were cycled in the voltage range of 3.0 - 4.6 V. Electrochemical data were tested using an Autolab potentiostat/galvanostat (PG302N). Data were analyzed for single peak fitting within the GSAS-II software.[2]

Calculations

Density functional theory (DFT) calculations were conducted using the Vienna ab initio Simulation Package (VASP)[7, 8] with the spin-polarized generalized gradient approximation (GGA) with the Perdew–Burke–Ernzerhof (PBE) exchange correlation.[9] The DFT+U method was introduced, and the value of U for Co was chosen as 3.3 eV that considers Van der Waals interactions. A kinetic energy cutoff of 450 eV was employed and the convergence threshold for atomic force during structural optimization was -0.05 eV Å^{-1}. The (104) $LiCoO_2$ surface (containing 50 Li atoms, 100 O atoms and 50 Co atoms) was modeled as a symmetric periodic slab with an 18 Å thick vacuum layer in the *c*-direction. In the supercell, the two bottom layers of Co, O, and Li atoms were kept fixed during calculations, while the others were allowed to relax. The N@P system was modelled by substituting 1 out of 50 Li (in the surface layer or the inner layer) with a P, and the O surrounding the P rearranged to form PO_4^{3-}. The migration pathway of Li$^+$ from one site to the adjacent site was calculated by the climbing image nudged elastic band (CI-NEB) method.
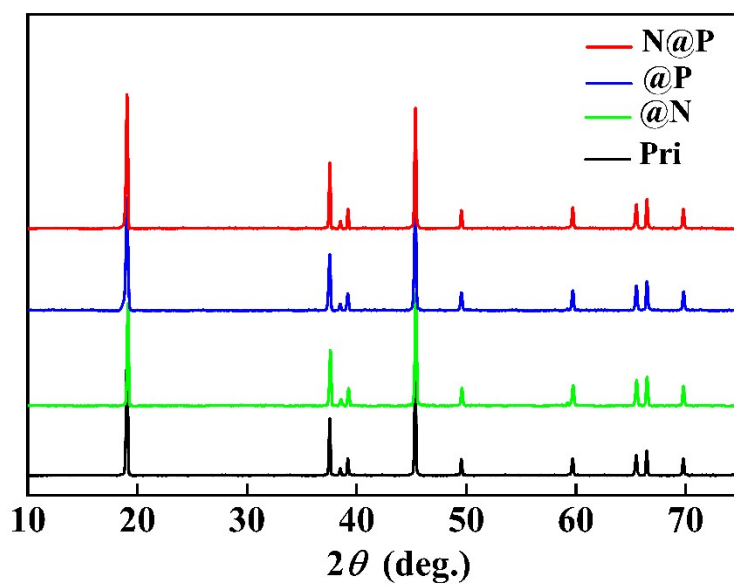
Figures

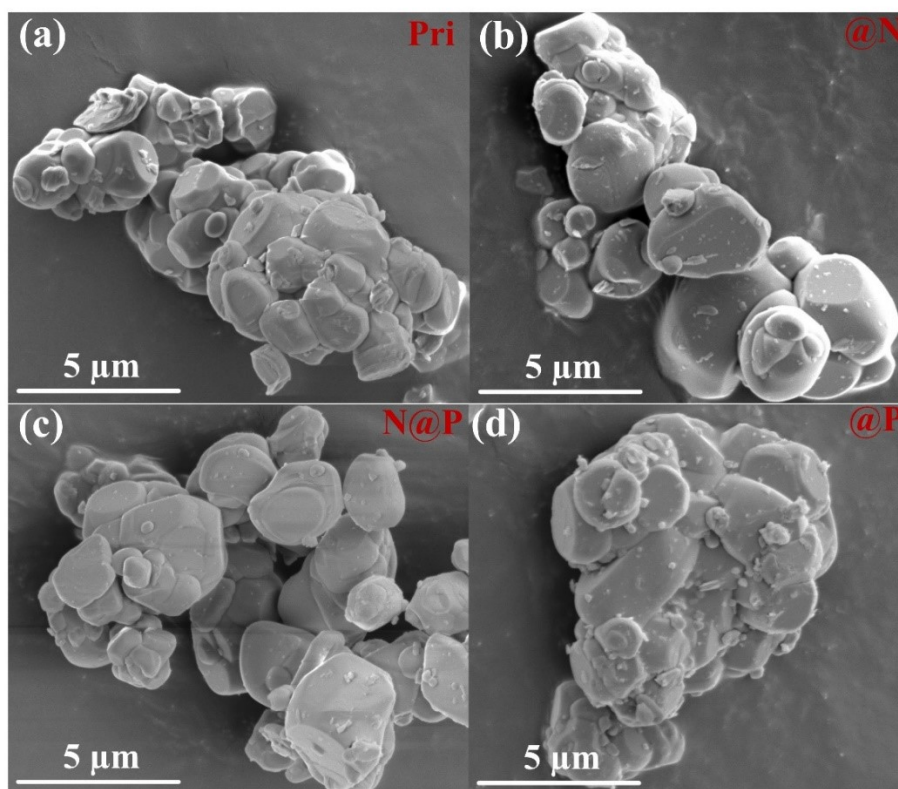**Fig. S1** Laboratory-based XRD data for the four samples.

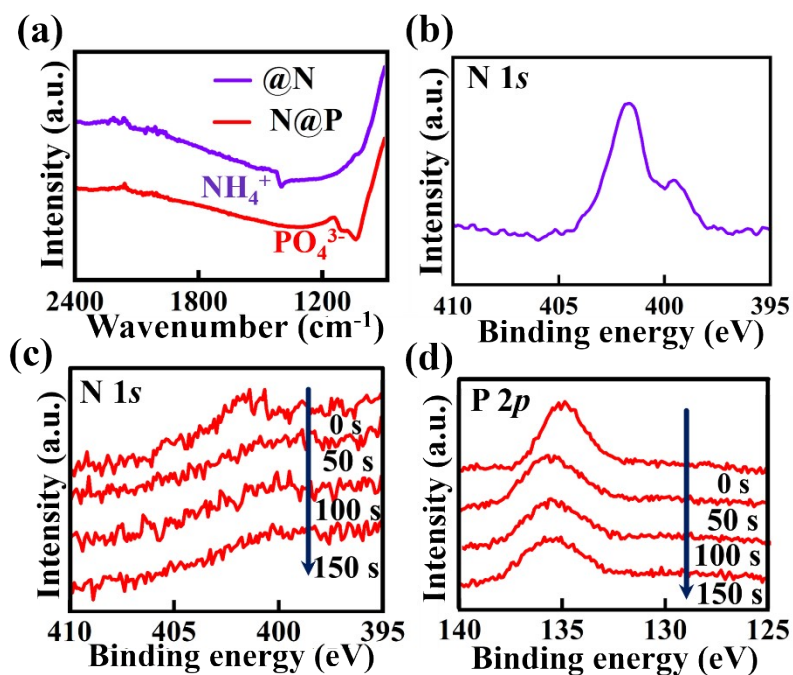**Fig. S2** SEM images of (a) Pri; (b) @N; (c) N@P; (d) @P.

Fig. S3 (a) FT-IR spectra for @N and N@P; (b) N 1s XPS spectrum of @N; Depth (time) dependent XPS spectra of N@P for (c) N 1s and (d) P 2p.
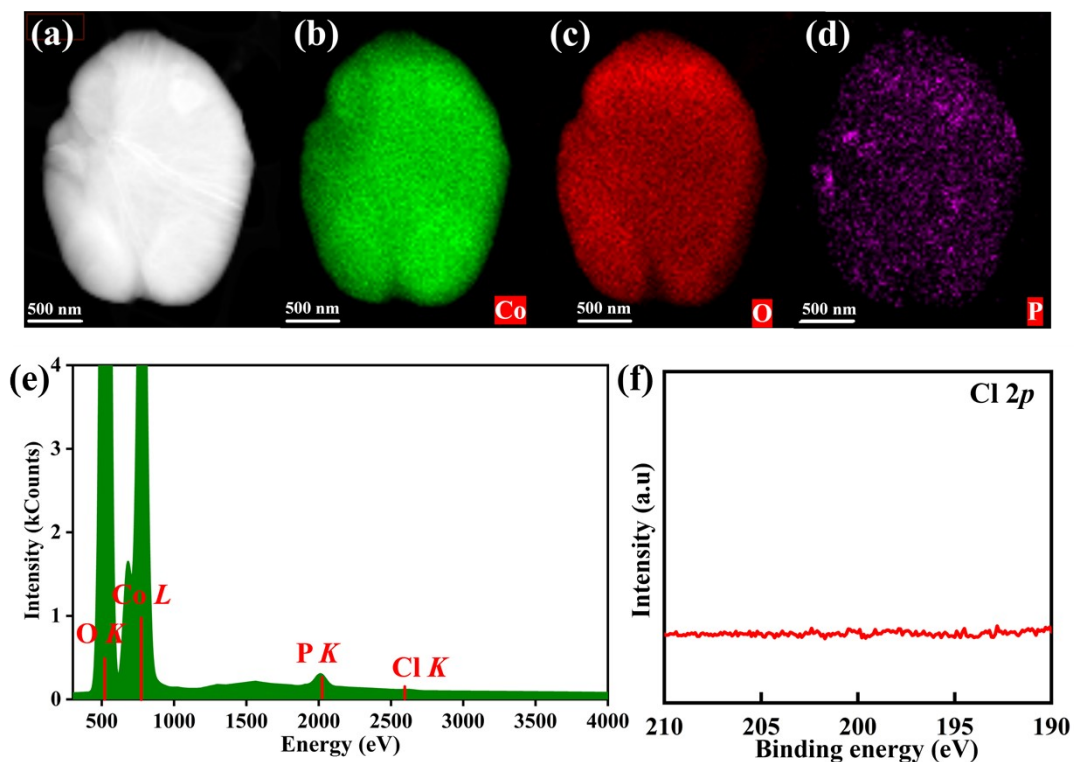

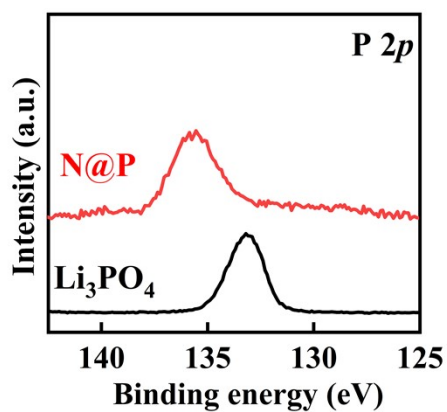**Fig. S4** (a-d) STEM EDS mapping results, (e) EDS spectra and (f) Cl 2p XPS spectra for N@P.
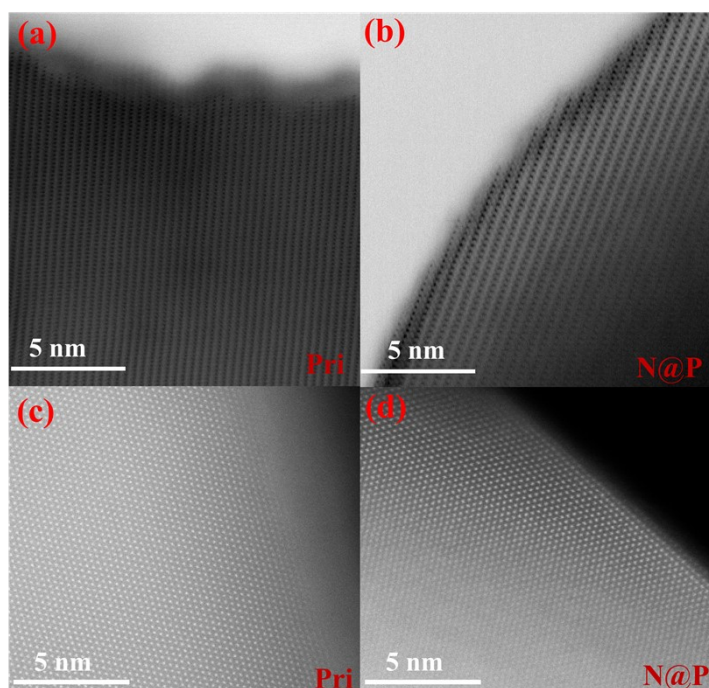
Fig. S5 XPS spectra of P 2*p* for N@P and Li$_3$PO$_4$.

Fig. S6 STEM images in ABF mode along the [010] of (a) Pri and (b) N@P; STEM images in HAADF mode along the [003] direction for (c) Pri and (d) N@P.
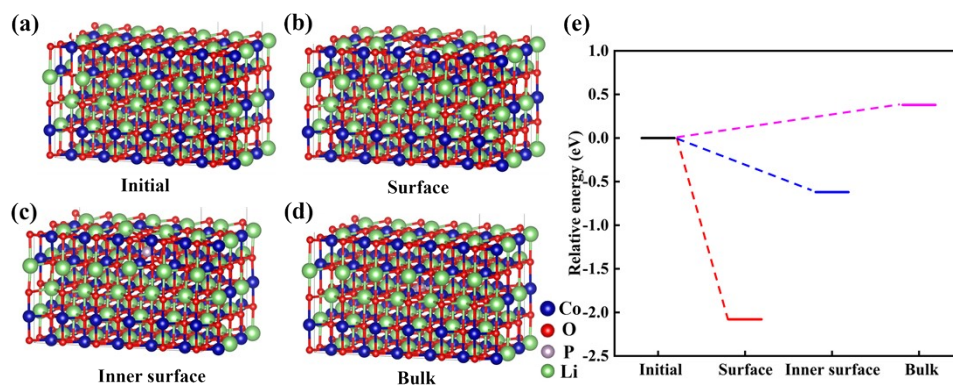
Fig. S7 Optimized atomic structure models of (a) bare $LiCoO_2$ (Initial), (b) PO_4^{3-} polyanionic species at the surface layer (Surface), (c) PO_4^{3-} polyanionic species in the inner surface layer (Inner surface), (d) PO_4^{3-} polyanionic species in the bulk structure (Bulk); (e) Relative energy for these models (The energy of initial structure is set to 0 eV).
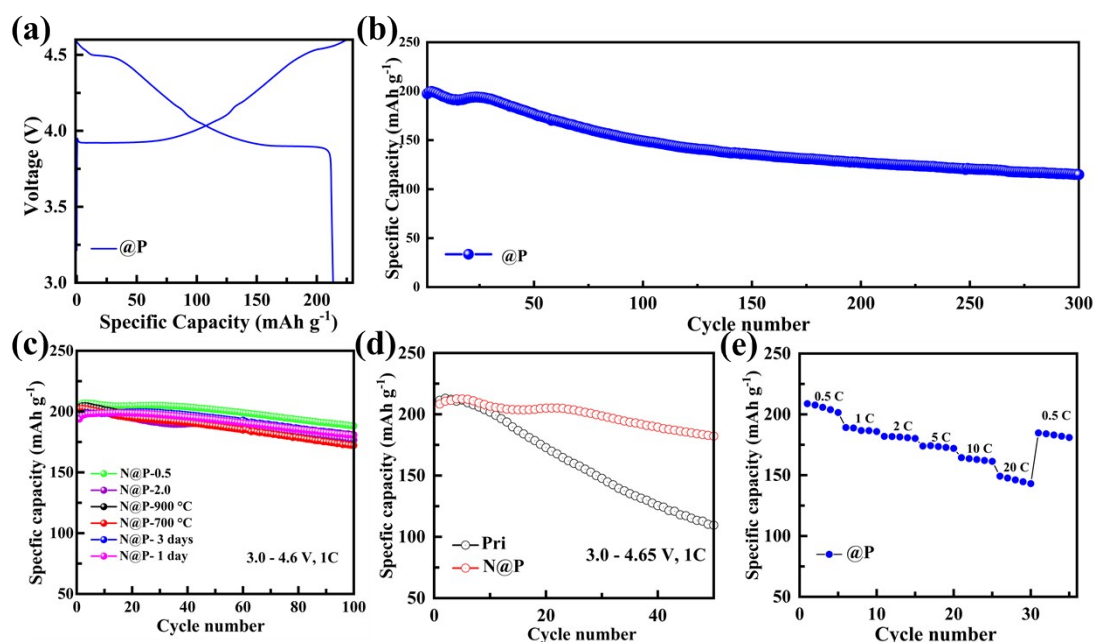

Fig. S8 (a) Charge-discharge profiles for @P at 0.1 C in the 1st cycle within 3.0 - 4.6 V; (b) Cycle stability of @P at 1 C over 300 cycles; (c) Cycle performance of modified samples with different experimental parameters at 1 C over 100 cycles; (d) Cycling stability of Pri and N@P at the current of 1 C and the voltage range of 3.0 - 4.65 V; (e) Rate capability of @P.

Fig. S8c shows the cycling performance of these samples after 100 cycles at the current of 1C and the voltage range of 3.0 - 4.6 V. The discharge capacity of N@P-1 day, N@P-

9

3 days, N@P-700 °C, N@P-900 °C, N@P-0.5, and N@P-2.0 are 198, 199, 202, 204, 206, 200 mAh g^{-1}, with corresponding capacity retention of 91%, 90%, 85%, 88%,91%, and 87% respectively. The capacity retentions for these samples surpass that of Pri (63%) and lowers than that of N@P (93%), which means that this surface engineering method could significantly enhance the electrochemical performance in high voltage LiCoO$_2$ and the parameters listed in the manuscript are the optimal selections.
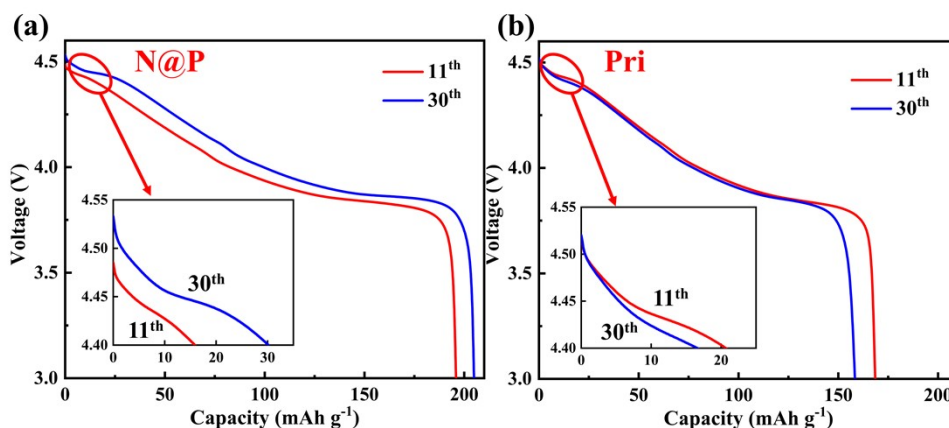

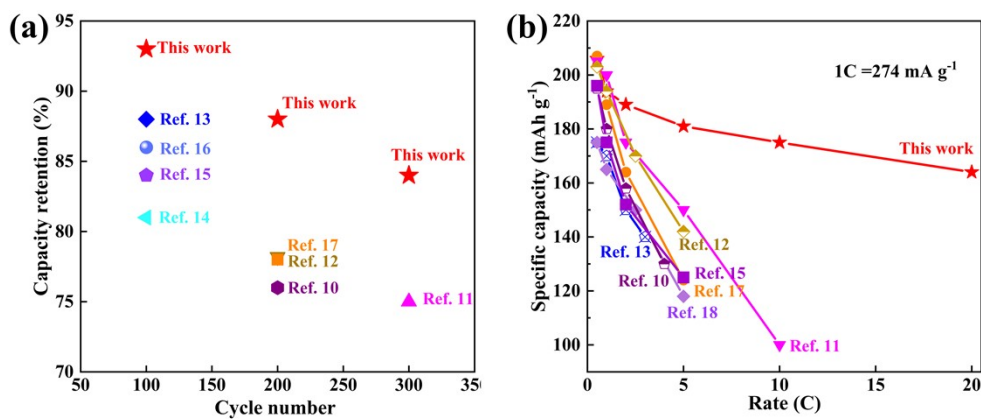**Fig. S9** The discharge curves for (a) N@P and (b) Pri at the 11th and 30th cycles.

Fig. S10 (a) Cycle and (b) rate performance comparison between N@P and other previously reported high voltage LiCoO$_2$.[10-18]
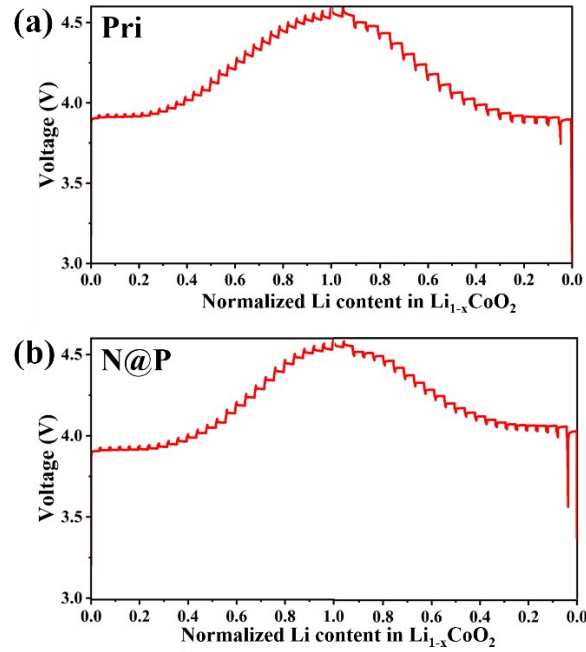
Fig. S11 GITT curves for (a) Pri and (b) N@P in the voltage range of 3.0 - 4.6 V.
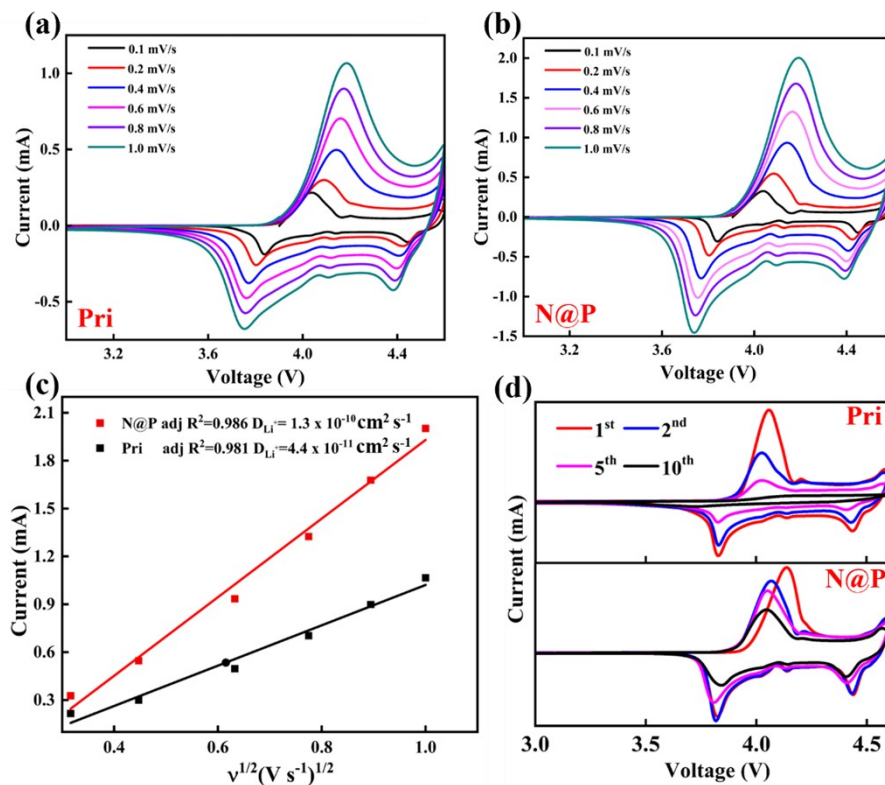

Fig. S12 CV curves of (a) Pri and (b) N@P at different scan rates; (c) Corresponding linear-fitting of peak current vs. square root of the scan rate for Pri and N@P; (d) CV curves for Pri and N@P at the scan rate of 0.1 mV s^{-1} in the different cycles.
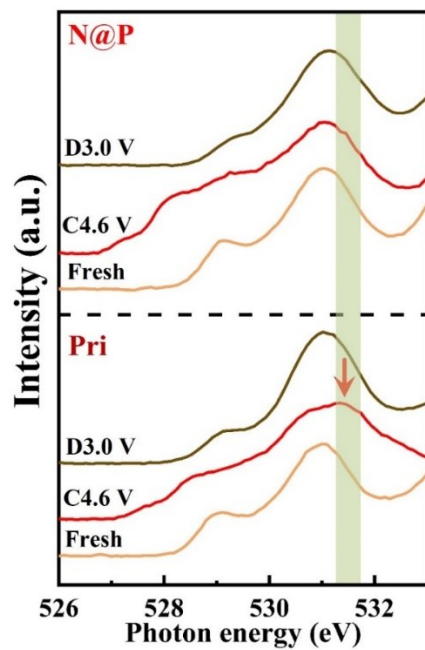
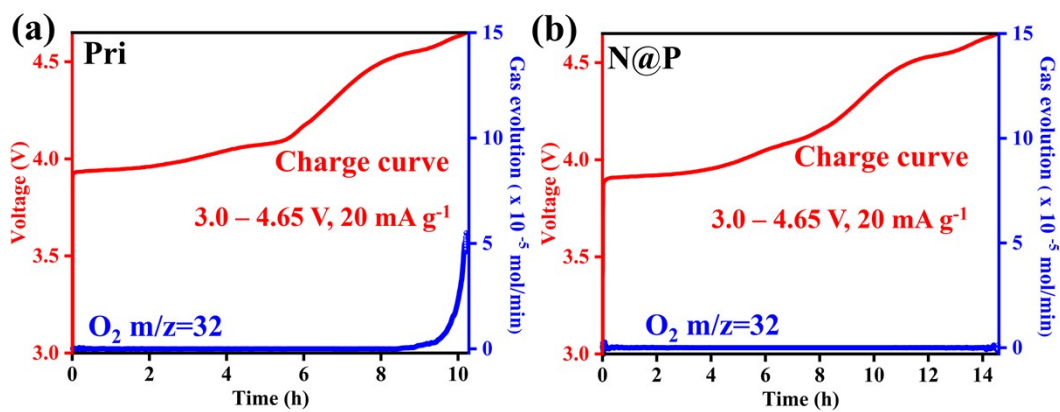**Fig. S13** O *K* edge spectra at different electrochemical states for N@P and Pri.

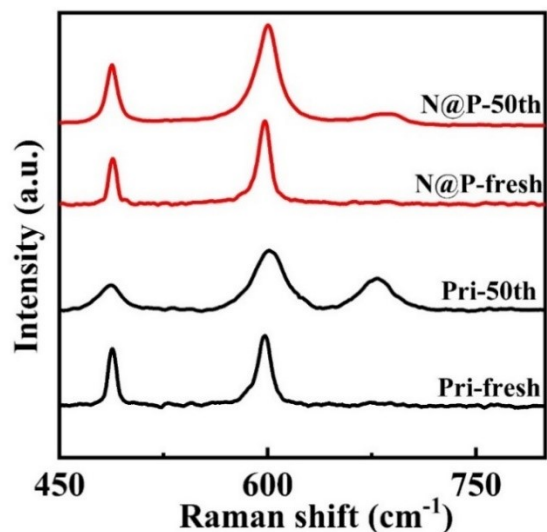**Fig. S14** O$_2$ gas evolution during the first charging process for (a) Pri and (b) N@P.

Fig. S15 Raman spectra for N@P and Pri in the fresh state and after 50 cycles.
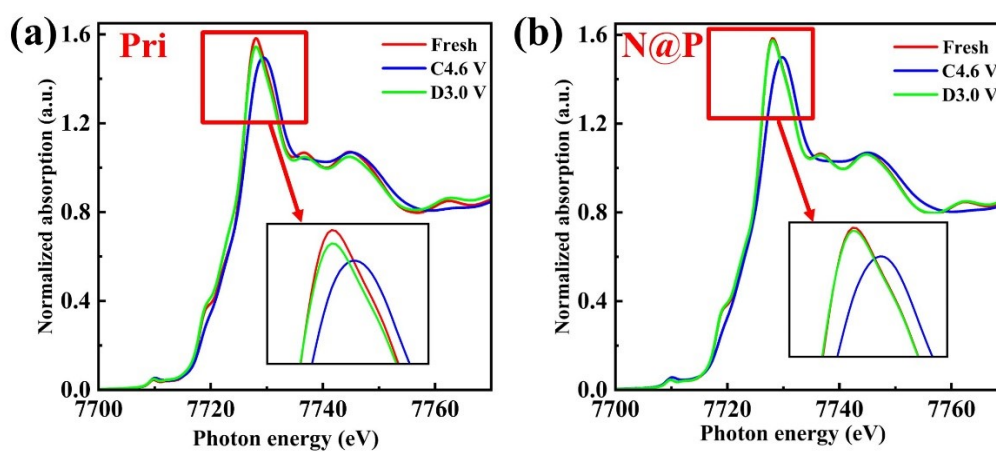
Fig. S16 XANES data at the Co *K* edge for (a) Pri and (b) N@P.
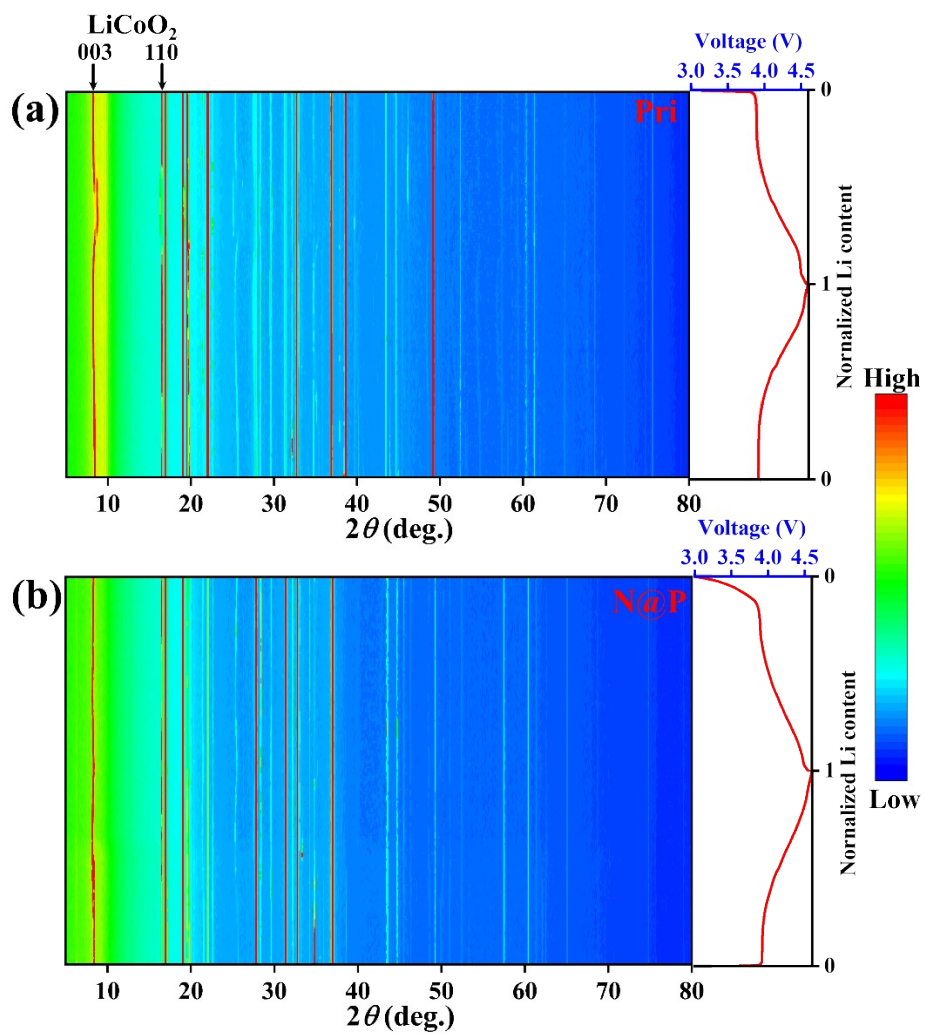
Fig. S17 Contour plot of *in situ* sXRPD data in the full 2θ angular range for (a) Pri and (b) N@P. Intensity is shown in color in the legend on the right.

Fig. S18 1D powder plots of 003 reflection for key positions at different Li-deintercalated content in $Li_{1-x}CoO_2$ for (a) Pri and (b) N@P.

Fig. S19 dQ/dV curve for N@P and Pri at the charge state.

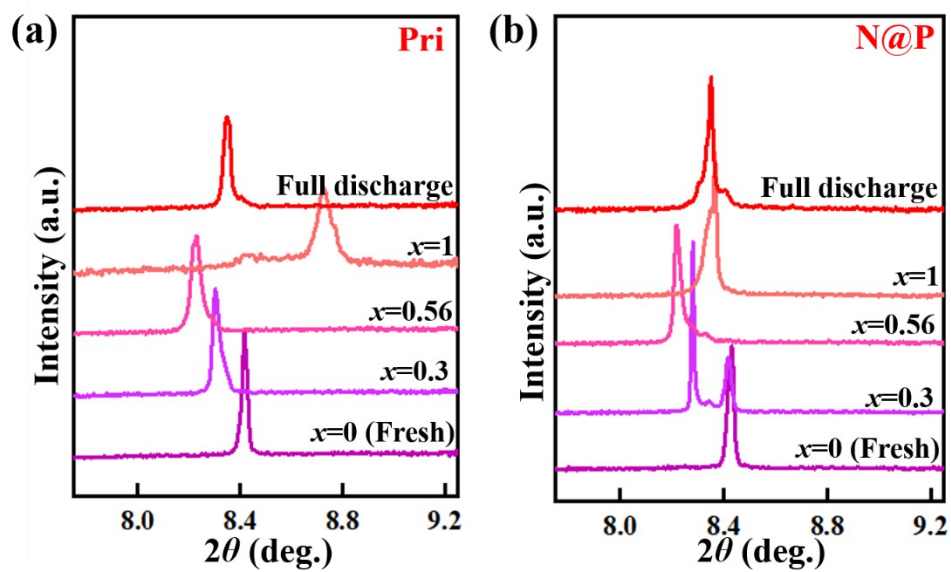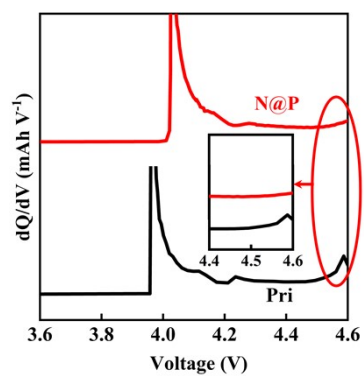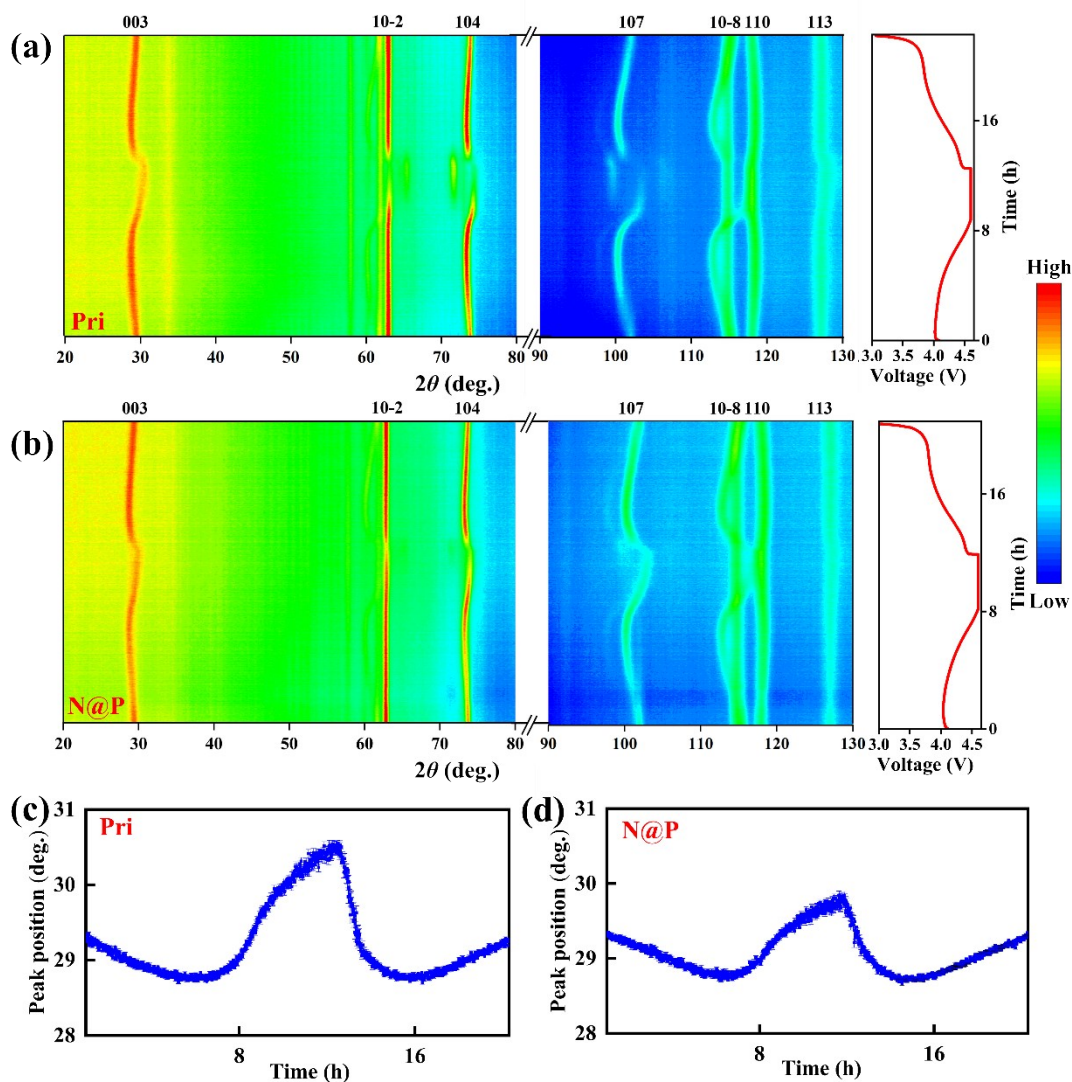**Fig. S20** Contour plot of *in-operando* NPD data in the full 2θ angular range for (a) Pri and (b) N@P pouch cells. Intensity is shown in color in the legend on the right. Results of single peak fitting of the 003 reflection of (c) Pri and (d) N@P.
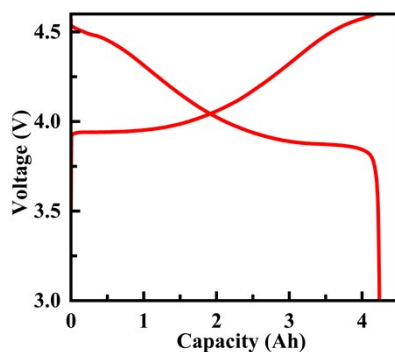
Fig. S21 Charge and discharge curve for pouch cell at the current of 200 mA g⁻¹ for the second cycle.

Tables

Table S1 Refined structure of Pri obtained from NPD data.

Pri-LiCoO$_2$ Space group Rm					
$a = b = 2.81555(5)$ Å, $c = 14.0643(1)$ Å, V = 96.555(1) Å^3					
Atom	x	y	z	Uiso	Site occupancy factor
Li	0	0	0	0.0098(5)	1.0
Co	0	0	0.5	0.0020(3)	1.0
O	0	0	0.23937(4)	0.0021(1)	1.0

Table S2 Refined structure of N@P using NPD data.

N@P-LiCoO$_2$ Space group Rm					
$a = b = 2.81585(6)$ Å, $c = 14.0677(2)$ Å, V = 96.599(2) Å^3					
Atom	x	y	z	Uiso	Site occupancy factor
Li	0	0	0	0.0119(8)	1.0
Co	0	0	0.5	0.0013(4)	1.0
O	0	0	0.23936(4)	0.0010(2)	1.0

Table S3 Summary of the reported electrochemical performances of LiCoO$_2$ with

doping modification.

Doping composition	Cycling performance (capacity, cycle number)	Ref.
Polyanionic PO_4^{3-} species	93%, 100th 88%, 200th 84%, 300th	This work
Cr	66%, 50th	19
Mg	84%, 100th	20
Gd	82.7%, 100th	21
W	72%, 100th	22
V	84%, 100th	23
Na-Ni	81%, 100th	14
Ti-F	75%, 100th	24
Ti-Mg-Al	86%,100th	16
Ti-Mg-B	78%, 100th	25
Na-Si-Al-F	84%, 200th	26

Table S4 Summary of the reported electrochemical performances of LiCoO$_2$ with coating modification.

Coating layer	Cycling performance (capacity, cycle number)	Ref.
Polyanionic PO$_4^{3-}$ species	93%, 100th 88%, 200th 84%, 300th	This work
Al$_2$O$_3$	88%, 200th	27
Pr$_6$O$_{11}$	80.3%, 200th	28
Li$_4$Ti$_5$O$_{12}$	89.9%, 100th	29
Li$_{1.5}$Al$_{0.5}$Ti$_{1.5}$(PO$_4$)$_3$	88.3%, 100th	15
LiFe$_{0.4}$Mn$_{0.6}$PO$_4$	85%, 200th	30
LiF and Li$_2$CoTi$_3$O$_8$	81.2%, 200th	13
LaPO$_4$ and Al$_2$O$_3$	87%, 200th	31
Li$_x$Co$_2$O$_4$ and Li$_2$SO$_4$	88%, 100th	32
LiMgPO$_4$/Li$_3$PO$_4$	73.4% ,200th	33

Table S5 Detailed parameters for pouch cell.

Parameters	Value for the pouch cell
Cathode mass loading	32 mg/cm^2
Thickness of Li metal	80 μm
Active material proportion	96%
E/C Ratio	1.6 g/Ah
Compaction density of cathodes side	2.56 g/cm^3
Pouch-cell weight	33.7 g
Capacity	4.24 Ah
Energy density	513 Wh/kg

References

1.   K.-D. Liss, B. Hunter, M. Hagen, T. Noakes and S. Kennedy, *Phys. B: Condens.*, 2006, **385-386**, 1010-1012.
2.   B. H. Toby and R. B. Von Dreele, *J. Appl. Crystallogr.*, 2013, **46**, 544-549.
3.   J. Feng, C. Wang, H. Lei, S. Liu, J. Liu, Y. Han, J. Zhang and W. Li, *Journal of Energy Chemistry*, 2023, **85**, 324-334.
4.   E. Gann, C. R. McNeill, A. Tadich, B. C. Cowie and L. Thomsen, *J. Synchrotron Radiat.*, 2016, **23**, 374-380.
5.   B. Ravel and M. Newville, *J. Synchrotron Radiat.*, 2005, **12**, 537-541.
6.   A. J. Studer, M. E. Hagen and T. J. Noakes, *Phys. B: Condens.*, 2006, **385-386**, 1013-1015.
7.   A. S. Botana and M. R. Norman, *Phys. Rev. Mater.*, 2019, **3**, 044001.
8.   G. Kresse and J. Hafner, *Phys. Rev. B Condens. Matter*, 1993, **47**, 558-561.
9.   P. E. Blochl, O. Jepsen and O. K. Andersen, *Phys. Rev. B Condens. Matter*, 1994, **49**, 16223-16233.
10. C. Yang, X. Liao, X. Zhou, C. Sun, R. Qu, J. Han, Y. Zhao, L. Wang, Y. You and J. Lu, *Adv. Mater.*, 2023, **35**, 2210966.
11. J. Zhang, P. F. Wang, P. Bai, H. Wan, S. Liu, S. Hou, X. Pu, J. Xia, W. Zhang, Z. Wang, B. Nan, X. Zhang, J. Xu and C. Wang, *Adv. Mater.*, 2022, **34**, e2108353.
12. L. Wang, J. Ma, C. Wang, X. Yu, R. Liu, F. Jiang, X. Sun, A. Du, X. Zhou and G. Cui, *Adv. Sci.*, 2019, **6**, 1900355.
13. S. Mao, Z. Shen, W. Zhang, Q. Wu, Z. Wang and Y. Lu, *Adv. Sci.*, 2022, **9**, 2104841.
14. P. Oh, J. Yun, J. H. Choi, G. Nam, S. Park, T. J. Embleton, M. Yoon, S. H. Joo, S. H. Kim, H. Jang, H. Kim, M. G. Kim, S. K. Kwak and J. Cho, *Adv. Energy Mater.*, 2022, **13**, 2202237.
15. Y. Wang, Q. Zhang, Z. C. Xue, L. Yang, J. Wang, F. Meng, Q. Li, H. Pan, J. N. Zhang, Z. Jiang, W. Yang, X. Yu, L. Gu and H. Li, *Adv. Energy Mater.*, 2020, **10**, 2001413.
16. J.-N. Zhang, Q. Li, C. Ouyang, X. Yu, M. Ge, X. Huang, E. Hu, C. Ma, S. Li, R. Xiao, W. Yang, Y. Chu, Y. Liu, H. Yu, X.-Q. Yang, X. Huang, L. Chen and H. Li, *Nat. Energy*, 2019, **4**, 594-603.
17. Z. Zhuang, J. Wang, K. Jia, G. Ji, J. Ma, Z. Han, Z. Piao, R. Gao, H. Ji, X. Zhong, G. Zhou and H. M. Cheng, *Adv. Mater.*, 2023, **35**, 2212059.
18. F. Zhang, N. Qin, Y. Li, H. Guo, Q. Gan, C. Zeng, Z. Li, Z. Wang, R. Wang, G. Liu, S. Gu, H. Huang, Z. Yang, J. Wang, Y. Deng and Z. Lu, *Energy Environ. Sci.*, 2023, **16**, 4345-4355.
19. M. Y. Meijing Zou, S. Gopukumar, and Jun-ichi Yamaki, *Chem. Mater.*, 2005, **17**, 1284-1286.
20. Y. Huang, Y. Zhu, H. Fu, M. Ou, C. Hu, S. Yu, Z. Hu, C. T. Chen, G. Jiang, H.

Gu, H. Lin, W. Luo and Y. Huang, *Angew. Chem. Int. Ed.*, 2021, **60**, 4682-4688.

21. S. Hao, Y. Li, S. Wang, J. Yang, Z. Tan, X. Li, X. Shen, X. Xi, J. Zheng and Z. He, *Mater. Today Energy*, 2022, **25**, 100980.

22. X.-H. Long, Y.-R. Wu, N. Zhang, P.-F. Yu, X.-F. Feng, S. Zheng, J.-M. Fu, X.-S. Liu, N. Liu, M. Wang, L.-M. Xu, J.-M. Chen and J.-M. Lee, *Chinese Physics B*, 2018, **27**.

23. W. Kong, D. Wong, K. An, J. Zhang, Z. Chen, C. Schulz, Z. Xu and X. Liu, *Adv. Funct. Mater.*, 2022, **32**, 2202679.

24. B. Shi, S. Hu, J. Feng, Y. Zhou, J. Liu, J. Zhang and W. Li, *J. Alloys Compd.*, 2022, **909**, 164787.

25. W. Shi, H. Dong, X. Feng, J. Yin, W. Sun, Y. Cheng and X. Xu, *Electrochim. Acta*, 2023, **464**, 142945.

26. Z. Zhang, Y. Meng and D. Xiao, *Energy Storage Materials*, 2023, **56**, 443-456.

27. R. Wu, T. Cao, H. Liu, X. Cheng, X. Liu and Y. Zhang, *ACS Appl Mater Interfaces*, 2022, **14**, 25524-25533.

28. Y. Huang, C. Xu, J. Gao, L. Shen, Q. Liu, G. Zhao, Q. Xie, Y. Lin, J. Li and Z. Huang, *Energy Environ. Mater.*, 2022, **6**, e12311.

29. C.-W. Wang, Y. Zhou, J.-H. You, J.-D. Chen, Z. Zhang, S.-J. Zhang, C.-G. Shi, W.-D. Zhang, M.-H. Zou, Y. Yu, J.-T. Li, L.-Y. Zeng, L. Huang and S.-G. Sun, *ACS Appl. Energy Mater.*, 2020, **3**, 2593-2603.

30. Y. Yan, S. Zhou, Y. Zheng, H. Zhang, J. Chen, G. Zeng, B. Zhang, Y. Tang, Q. Zheng, C. Wang, C. W. Wang, H. G. Liao, I. Manke, X. Kuai, K. Dong, Y. Sun, Y. Qiao and S. G. Sun, *Adv. Funct. Mater.*, 2023, **34**, 2310799.

31. Y. Zou, Y. Xiao, Y. Tang, Y. Cheng, S.-G. Sun, M.-S. Wang, Y. Yang and J. Zheng, *J. Power Sources*, 2023, **555**, 232409.

32. W. Huang, Q. Zhao, M. Zhang, S. Xu, H. Xue, C. Zhu, J. Fang, W. Zhao, G. Ren, R. Qin, Q. Zhao, H. Chen and F. Pan, *Adv. Energy Mater.*, 2022, **12**, 2200813.

33. J. Zhong, W. Zhao, M. Zhang, Z. W. Yin, Z. Zhuo, S. Zhang, M. Zhang, F. Pan, B. Zhang and Z. Lin, *Small*, 2023, **19**, e2300802.